P H Y S I C A L R E V I E W L E T T E R S

Multiple Time Scales in Diffraction Measurements of Diffusive Surface Relaxation

Aaron Fleet,[1,2] Darren Dale,[3,2] A. R. Woll,[4] Y. Suzuki,[5] and J. D. Brock[1,2]

[1]*School of Applied and Engineering Physics, Cornell University, Ithaca, New York 14853, USA*
[2]*Cornell Center for Materials Research, Cornell University, Ithaca, New York 14853, USA*
[3]*Department of Materials Science and Engineering, Cornell University, Ithaca, New York 14853, USA*
[4]*Cornell High Energy Synchrotron Source, Cornell University, Ithaca, New York 14853, USA*
[5]*Department of Materials Science and Engineering, UC Berkeley, Berkeley, California 94720, USA*

We grew $SrTiO_3$ on $SrTiO_3$(001) by pulsed laser deposition, using x-ray scattering to monitor the growth in real time. The time-resolved small-angle scattering exhibits a well-defined length scale associated with the spacing between unit-cell high surface features. This length scale imposes a discrete spectrum of Fourier components and rate constants upon the diffusion equation solution, evident in multiple exponential relaxation of the "anti-Bragg" diffracted intensity. An Arrhenius analysis of measured rate constants confirms that they originate from a single activation energy.

Despite decades of study, a complete description of the fundamental mechanisms that control a broad class of epitaxial growth techniques persists as a challenging problem in nonequilibrium physics. One question concerns the evolution of a film surface following the arrival of newly deposited species. The surface may relax via multiple processes, including molecular formation and diffusion [1]. A growth technique such as pulsed laser deposition (PLD), which utilizes a plume of laser-ablated material to instantaneously deposit a high concentration of species onto an atomically smooth surface [2], facilitates observation of the postdeposition relaxation. Many fine diffraction-based studies [1,3–5] of this relaxation have revealed multiple time scales in the postpulse intensity transient, leading authors to suggest that several nondegenerate mechanisms govern the surface's approach to equilibrium. However, as we demonstrate in this Letter, multiple time scales in diffraction data do not provide sufficient evidence of multiple physical processes during surface relaxation. Furthermore, by combining elementary diffusion theory with kinematic scattering theory, we show that classical diffusion alone produces a nonexponential diffraction response during PLD.

In the simplest film-growth model, deposited particles diffuse on a substrate surface until they either evaporate, attach to existing step edges, or collide and nucleate islands, to form a film [6,7]. Depending on the substrate temperature and specific energy barriers, films grow in either 3D, layer-by-layer, or step-flow modes [8–10]. These modes may be subdivided into myriad subcategories pertaining to different atomic-scale morphologies. By scattering x rays from the film surface, one may determine the specific morphology for a given film-growth system, for example, the technologically interesting system of $SrTiO_3$ (STO) homoepitaxy.

To obtain information regarding morphological evolution in this system, we measured the small-angle x-ray scattering (SAXS) during STO PLD (Fig. 1). A CCD detector recorded both the specular x rays associated with out-of-plane atomic positions and the diffuse x rays associated with in-plane correlations. Previous studies have taken advantage of this technique to study simultaneous in- and out-of-plane processes [11].

During STO homoepitaxy, we observed that the diffuse and specular signals oscillate at the same frequency, but out of phase. The specular oscillations indicate layer-by-layer growth of the STO film [12], while the diffuse peak oscillations indicate the appearance and disappearance of an in-plane feature. During growth of the first monolayer, the diffuse peaks are separated by $\Delta q_\parallel \approx 0.06$ Å^{-1} (inset of Fig. 1). This indicates that a characteristic length scale of ~200 Å develops as the growing layer nears half comple-

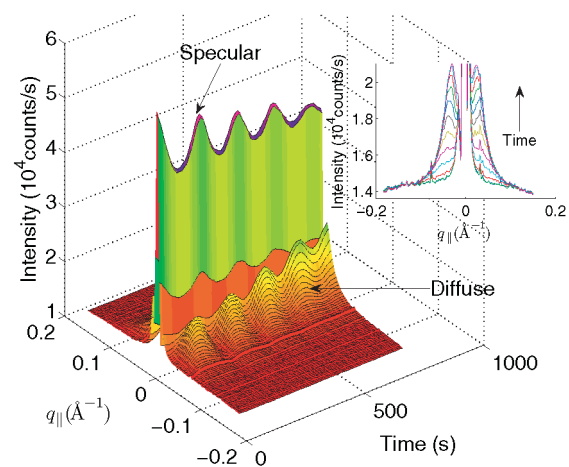FIG. 1 (color). X-ray intensity measured around $(00\frac{1}{5})$ during $SrTiO_3$ homoepitaxy at $T = 970$ K, $P_{O_2} = 10^{-5}$ torr, and $f = 0.1$ Hz. An absorber attenuated the specular beam. Inset: Diffuse intensity during deposition of the first half monolayer. Each curve represents the integrated signal following a pulse.

tion, and vanishes at layer completion. This length scale increases slightly with increasing film thickness, eventually preventing resolution of the diffuse and specular signals.

While the presence of a distinct diffuse peak indicates a well-defined surface length scale, the peak profile contains little information regarding feature shapes or size distributions [13]. To associate the length scale with a specific surface structure, we obtained real-space information via *ex situ* atomic force microscopy (AFM) (Fig. 2). The micrographs reveal the morphology of the deposited film to be dominated by holes in a narrow size distribution, peaked at 20 nm. This morphology is consistent with AFM images in the literature [12].

Combining the x-ray and AFM information, we interpret the diffuse oscillations to indicate the nucleation and coalescence of unit-cell high islands. The diffuse peak indicates a short-range order to the nucleation density of $\sim$50 unit cells ($a_{STO} = 3.905$ Å). The nearly constant value of $q_{\parallel}$ (during the first monolayer) of the diffuse peaks indicates that while islands grow in size as new material arrives, little subsequent nucleation occurs after the first pulse. As islands coalesce, the diffuse signal corresponds to holes in the surface that fill as the specular intensity approaches a maximum. Because of the kinetics of hole filling (discussed below), small holes fill very slowly, so that the film surface comes to be dominated by a network of similarly sized small holes.

The time scales associated with material incorporation and diffusion are regulated by the substrate temperature T, surface morphology, and diffusion energy barrier U (and possibly by the kinetic energy of incident particles [14]). While rate-equation models [12,15] describe diffusion in terms of *interlayer* transport of deposited material, the following argument demonstrates that *intralayer* diffusion is a key component of the surface kinetics.

In a continuum model of diffusion, the surface density ρ of diffusing species evolves according to the diffusion equation: $\frac{\partial \rho}{\partial t} = D\nabla^2\rho$. The diffusion coefficient, D, depends on T and U, via $D \propto e^{-U/k_B T}$ [6]. The Fourier transform of the diffusion equation yields $\rho_q \propto e^{-Dq^2 t}$, where q corresponds to the spatial frequencies present in ρ. In a
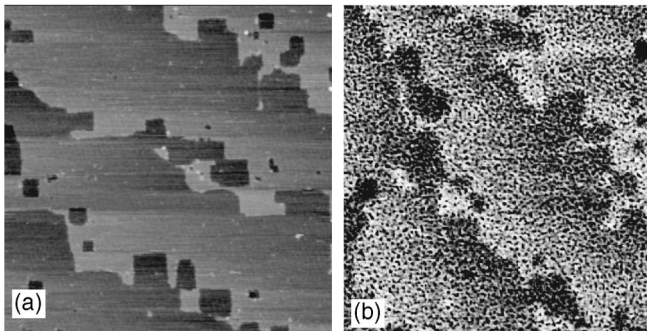

FIG. 2.   AFM images (1 μm $\times$ 1 μm) of etched STO substrate before (a) and after (b) deposition of 42 layers of STO.

boundary value problem, one expects a discrete spectrum of rate constants $k \propto -Dq^2$. Short wavelength modes decay rapidly, and the spatial geometry determines the k spectrum. We emphasize that a single energy U gives rise to multiple rate constants k.

The combined SAXS (Fig. 1) and AFM data suggest a film morphology of round islands and holes. We therefore solve the diffusion equation in a circular region of the (nonmiscut) substrate of radius r_b, with a step located at $r_a < r_b$. We write the solution as $\rho(r, \phi, t) = X(r, \phi)e^{-kt}$, and specify $X_<$ and $X_>$ as the spatial solutions in the regions $0 < r < r_a$ and $r_a < r < r_b$, respectively. Assuming $\frac{\partial \rho}{\partial \phi} = 0$, X takes the form of Bessel, $J_0(r)$, and Neumann, $N_0(r)$, functions.

We assume the step acts as a perfect sink, providing a boundary condition $\rho(r_a) = 0$ [6,7]. This method neglects the possible energy barrier for particles to cross downward over the step. One can incorporate this "Ehrlich-Schwoebel barrier" by specifying the particle current $\vec{j} = -D\vec{\nabla}\rho$ at the boundary [16,17], without changing the conclusions of this Letter.

The $X_<$ exclude the $N_0(r)$, which diverge as $r \to 0$:

$$X_< = \sum_m A_m J_0(\alpha_m r) \equiv \sum_m X_{m<}.$$

Here $\alpha_m r_a$ is the mth root of $J_0(r)$.

We further assume that $\frac{\partial \rho}{\partial r}\big|_{r_b} = 0$, i.e., that the system boundary is far from any steps. Then

$$X_> = \sum_m B_m J_0(\beta_m r) + C_m N_0(\beta_m r) \equiv \sum_m X_{m>},$$

where the boundary conditions determine the β_m and the ratio $\frac{B_m}{C_m}$. Finally, we specify $\rho(t = 0, r) = \sigma_0$, where σ_0 is the coverage of a single pulse. This sets A_m and B_m via the orthogonality of the $J_0(r)$ and $N_0(r)$.

Kinematic theory accurately describes the scattered intensity. For the simple case of momentum transfer normal to the surface of a nonmiscut crystal, one has, in homoepitaxy [18],

$$I(t) \propto |F(q)|^2 \left| \frac{1}{1 - e^{iqd}} + \sum_n \theta_n(t)e^{-iqnd} \right|^2. \quad (1)$$

Here q is the scattering vector, $F(q)$ is the scattering amplitude of a single layer, $\theta_n(t)$ is the time-dependent coverage of the nth layer, and d is the layer spacing. The first term represents the scattering from an ideally terminated single crystal. The second term represents the scattering from the deposited film. At the anti-Bragg position, x rays scattered from adjacent layers interfere destructively, providing maximum sensitivity to single step height fluctuations.

Combining the complete solution $\rho(r, t)$ with Eq. (1), we calculate the anti-Bragg x-ray intensity, $I(t)$:

$$I(t) \propto \left(\frac{1}{2} - \theta_0 - \sigma_0 + 2\sum_m \sigma_m e^{-Dq_m^2 t} \right)^2, \qquad (2)$$

where σ_0 is the coverage of single pulse. The prepulse surface coverage, θ_0, the coverages σ_m of species in the mass-losing layer, and the choice $q_m = \alpha_m$ or β_m depend on whether the step at r_a bounds an island or a hole. The complicated time dependence of Eq. (2) involves multiple rate constants $k_m = Dq_m^2$.

At the nucleation of each new layer, the morphology is characterized by islands. In this regime, $\theta_0 = (\frac{r_a}{r_b})^2$, $\sigma_m = \frac{2}{r_b^2} \int_0^{r_a} X_{m<}(r) r dr$, and $q_m = \alpha_m$. Only species transferring off of the island affect I, so that $X_>$ does not influence the time dependence.

In this case, I slightly decreases following the large instantaneous drop due to pulse arrival [Fig. 3(a)]. The growing layer moves toward half completion and a minimum in the anti-Bragg oscillation. The diffusion-moderated change is small, since most of the deposited material does not land on the island. The small fractions of total deposited material, $\frac{\sigma_m}{\sigma_0}$, transferring between layers, move at relatively rapid rates k_m [inset of Fig. 3(a)]. Many researchers have observed intensity transients in qualitative agreement with this form [4,12].

As the islands grow and coalesce, a network of holes better describes the surface. Here, $\theta_0 = 1 - (\frac{r_a}{r_b})^2$, $\sigma_m = \frac{2}{r_b^2} \int_{r_a}^{r_b} X_{m>}(r) r dr$, and $q_m = \beta_m$. The intensity rises substantially following the instantaneous drop, as the film moves closer to the layer completion condition and growth oscillation maximum [Fig. 3(b)]. The k_m are in general slower than in the island case. Roughly 80% of deposited material is in the mode associated with $X_{0>}$, with a time constant $\frac{1}{k_0}$ equal to a few seconds [inset of Fig. 3(a)]. Of

the species transferring into the hole, $\sim$10% move at rates $k_m \gg k_0$, adding faster components to the intensity change, noticeable at early times.

To test the model, we measured the anti-Bragg intensity during STO homoepitaxy via PLD (Fig. 4), under conditions which promote steady-state layer-by-layer growth [10]. Our PLD chamber is an integral component of a fully featured x-ray diffractometer that is permanently installed in the G3 hutch of the Cornell High Energy Synchrotron Source (CHESS) [14]. By controlling the chamber oxygen pressure, P_{O_2}, substrate temperature, T, and laser repetition rate, f, we can select different growth modes, while monitoring film growth *in situ* with x rays. We grew STO films on STO (001) substrates with $P_{O_2} = 10^{-6}$ torr, $T = 900 \to 1060$ K, and $f = 0.1$ Hz. We set the laser energy density at the single crystal STO target to 2–3 J/cm^2, and the target-substrate distance to 6 cm, for an average $\sigma_0 \approx 0.1$ monolayer/pulse.

To obtain the required time resolution, we recorded $I(t)$ with a multichannel scaler (MCS) set to 10 ms dwell time per channel. The MCS triggered the laser at the midpoint of each pass, collecting 5 s of intensity before and after each laser pulse. We then normalized each MCS pass by $I(t)$ integrated over the prepulse region [14].

We typically measured anti-Bragg intensities of 10^4 counts/s. This signal strength yields 10% statistical noise in each MCS bin, comparable to the signal change $\frac{\Delta I}{I}$. To reduce the noise, we averaged normalized MCS passes for a given sample over the entire deposition [14]. While improving counting statistics, this method sacrifices information by combining intensity transients from a range of surface morphologies. For example, during the growth of the first half monolayer, individual transients resemble the curve of Fig. 3(a) (noise prevents quantitative analysis).
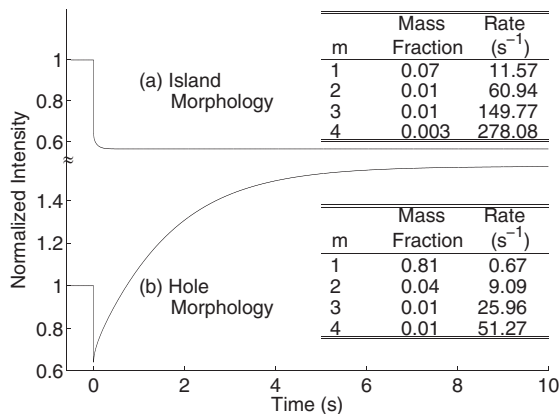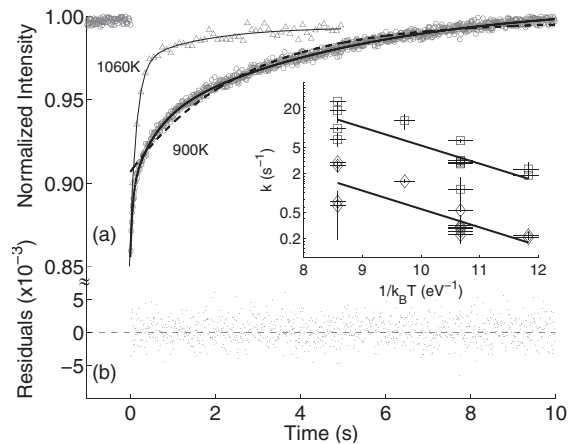

FIG. 3.　Calculated anti-Bragg x-ray intensity following a laser pulse, using Eq. (2) and parameters in agreement with experiment. The normalized intensity drops instantaneously upon pulse arrival, and then either falls (a) or rises (b), depending upon surface morphology. Tables in each case list fractions of total deposited mass, $\frac{\sigma_m}{\sigma_0}$, and diffusion rates of the first four modes. Integral forms of σ_m were evaluated numerically.

FIG. 4.　(a) Fits of Eq. (3) to 900 K ($\bigcirc$) and 1060 K ($\triangle$) data with one (dashed curve) and three (solid curve) rate constants. Marker size roughly equals the error of each point. (b) Residuals of the 900 K fit with three rate constants. Inset: Arrhenius plot of 13 samples, with $T = 900 \to 1060$ K, and $P_{O_2} = 10^{-6}$ torr. Ordinate is k_1 ($\diamondsuit$) and k_2 ($\square$) of Eq. (3).

However, sums of MCS passes at constant growth oscillation phase reveal the transient to resemble the curve of Fig. 3(b) at all phases [14]. This suggests that a hole morphology dominates throughout much of the growth. A numerical simulation of a system containing an island and a hole reveals that the holes dictate the time structure of the intensity transient. One can crudely predict this result by summing the two curves of Fig. 3. Numerous authors have observed rising intensity transients during the "falling" portion of the anti-Bragg oscillation, where one might expect an island morphology [1,3,4].

To fit the data, we truncated the series of Eq. (2) at $m = 3$, for which the model predicts the $k_{m>3}$ to be much greater than $f_{\mathrm{Nyquist}} = 50$ Hz. In the hole regime, we have $\sigma_m \ll 1$. Retaining small quantities to first order,

$$I(t) = a - \sum_{m=1}^{3} b_m e^{-k_m t}. \qquad (3)$$

We fit Eq. (3) to data from 13 samples grown under layer-by-layer conditions. For samples grown at $T > 970$ K, we required only two rate constants, suggesting that $k_3 \gg f_{\mathrm{Nyquist}}$ at high T. A typical fit [Fig. 4(a)] describes the data well, with $\chi_\nu^2 = 1.1$ and normally distributed residuals [Fig. 4(b)]. Adding terms $m > 3$ did not improve χ_ν^2. For comparison, we also show a fit with the series truncated at $m = 1$, a form often assumed for the intensity evolution [1,4]. This simple exponential clearly fails to describe the data at early times ($\chi_\nu^2 = 4.9$).

Averaged over all samples, the ratio $\frac{k_2}{k_1} = 11.9$ agrees with the hole model prediction of 9 to 13, which can vary depending on hole size and shape. The ratio $\frac{k_3}{k_1} = 80$ exceeds the hole model prediction of 30. This may be due to a small island contribution, for which $\frac{k_{2,\mathrm{island}}}{k_{1,\mathrm{hole}}} \approx 100$. Additionally, the fixed r_a approximation used to derive Eq. (2) decreases the ratio $\frac{k_{m>1}}{k_1}$. In reality, the holes fill in, effecting longer saturation times for the x-ray intensity and reducing the measured k_1.

The ratio $\frac{b_1}{b_2} \approx 2$ is smaller than the model prediction of 10. High frequency terms thus contribute more to the signal than predicted. This discrepancy could arise from the approximation of a two-level system. As growth proceeds, new layers nucleate before tiny holes in underlying levels completely fill in. This broadening of the growth interface effects greater deposition near step edges, increasing interlayer transfer proportionately.

In the inset of Fig. 4, we present k_1 and k_2 in an Arrhenius plot for the 13 samples mentioned above. Since $k_m \propto D$, the slopes of linear fits give the diffusion activation energy, U. The slopes of separate fits of k_1 and k_2 agree to within 1%, revealing that both rates arise from a single energy. A simultaneous fit yields $U = 0.6 \pm 0.2$ eV, at the low end of the range (< 0.5 to > 3 eV) of published diffusion barriers for oxides [1,3,4]. Measured diffusion barriers increase with oxygen pressure, possibly because

highly kinetic plume particles thermalize via gas collisions [4]. Our U may underestimate the actual diffusion activation energy due to our low oxygen pressure.

That a single diffusion process generates multiple time scales in the diffracted intensity is a direct consequence of the characteristic length scale on the surface, revealed in our SAXS and AFM data. This length scale forces a discrete q spectrum upon the density of diffusing species. Higher-q components decay quickly as particles diffuse to steps, effecting a rapid early response in the time-resolved anti-Bragg intensity. The observation of multiple time scales in diffraction data cannot therefore be used to infer multiple physical processes.

[1] H. Karl and B. Stritzker, Phys. Rev. Lett. **69**, 2939 (1992).

[2] P. R. Willmott and J. R. Huber, Rev. Mod. Phys. **72**, 315 (2000).

[3] M. Lippmaa, N. Nakagawa, M. Kawasaki, S. Ohashi, and H. Koinuma, Appl. Phys. Lett. **76**, 2439 (2000).

[4] D. Blank, G. Koster, G. Rijnders, E. van Setten, P. Slycke, and H. Rogalla, Appl. Phys. A **69**, S17 (1999).

[5] T. Wang, J. Juang, K. Wu, T. Uen, and Y. Gou, Jpn. J. Appl. Phys. **43**, 771 (2004).

[6] W. Burton, N. Cabrera, and F. Frank, Philos. Trans. R. Soc. London **243**, 299 (1951).

[7] G. Petrich, P. Pukite, A. Wowchak, G. Whaley, P. Cohen, and A. Arrott, J. Cryst. Growth **95**, 23 (1989).

[8] S. Metev and K. Meteva, Appl. Surf. Sci. **43**, 402 (1989).

[9] J. H. Neave, P. J. Dobson, B. A. Joyce, and J. Zhang, Appl. Phys. Lett. **47**, 100 (1985).

[10] J. Song and Y. Jeong, Solid State Commun. **125**, 563 (2003).

[11] D. Kisker, G. Stephenson, J. Tersoff, P. Fuoss, and S. Brennan, J. Cryst. Growth **163**, 54 (1996).

[12] G. Eres, J. Z. Tischler, M. Yoon, B. C. Larson, C. M. Rouleau, D. H. Lowndes, and P. Zschack, Appl. Phys. Lett. **80**, 3379 (2002).

[13] A. Guinier, *X-Ray Diffraction in Crystals, Imperfect Crystals, and Amorphous Bodies* (Dover, New York, 1994).

[14] A. Fleet, D. Dale, Y. Suzuki, and J. D. Brock, Phys. Rev. Lett. **94**, 036102 (2005).

[15] P. Cohen, G. Petrich, P. Pukite, G. Whaley, and A. Arrott, Surf. Sci. **216**, 222 (1989).

[16] J. Tersoff, A. W. DeniervanderGon, and R. M. Tromp, Phys. Rev. Lett. **72**, 266 (1994).

[17] R. Ghez and S. Iyer, IBM J. Res. Dev. **32**, 804 (1988).

[18] B. M. Ocko, D. Gibbs, K. G. Huang, D. M. Zehner, and S. G. J. Mochrie, Phys. Rev. B **44**, 6429 (1991).